

Paper 067

WIND TUNNEL OPEN SECTION CHARACTERIZATION FOR ROTORCRAFT TESTS

M. Biava¹, G. Campanardi², G. Gibertini², D. Grassi², L. Vigevano², A. Zanotti²

¹ AWPARC, Milano, Italy ² Dipartimento di Ingegneria Aerospaziale - Politecnico di Milano, Via La Masa 34, 20156 Milano, Italy

Abstract

The paper presents an experimental and numerical characterization of the flow inside the open test section of the Politecnico di Milano large wind tunnel, when operating a model rotor in forward flight conditions. The numerical simulations are carried out in steady conditions by representing the rotor by means of an actuator disk model. The combined analysis of measured and computed data allows to investigate the possible occurrence of flow breakdown in terms of wind tunnel speed and rotor thrust.

1 Introduction

Despite the increasing capability of CFD methods in predicting rotor performance, the use of wind tunnel test measurements still plays an important role in the design of new rotor systems. However, it is not obvious how to operate the model rotor and the wind tunnel so as to reproduce closely free air conditions. In fact, rotor tests at low speed and high thrust in a wind tunnel may experience what is known as *flow breakdown*, that happens when the interaction between the rotor wake and the tunnel walls strongly modifies the flow in the vicinity of the rotor due to the formation of recirculating flow regions [1]. In flow breakdown condition the wind tunnel environment is no more representative of the free air environment and the rotor performance cannot be adjusted by means of wall corrections. Therefore, such operating conditions are to be avoided in a test campaign.

Shinoda [2] addressed the study of wall interference effects and the identification of flow breakdown by means of an extensive experimental campaign in the 80×120 foot closed-section wind tunnel at NASA Ames. In open wind tunnel sections, due to a limited experimental data base, it is still unclear how to define the flow breakdown regime. Data reported in [3] seem to show that at low advance ratio values the rotor power

gathered in both closed and open sections collapses into a single curve, thus suggesting the occurrence of flow breakdown, but the matter needs to be further investigated. To this aim, a campaign of experimental measurements and numerical simulations has been carried out to characterize the flow field in the 4×3.8 m open test section of the Politecnico di Milano (PoliMi) large wind tunnel, generated by the AgustaWestland AW139 model rotor. The computations were performed with the CFD code *ROSITA* (ROtorcraft Software ITAly)[4],[5], based on the solution of the Reynolds Averaged Navier-Stokes equations coupled with the one-equation turbulence model of Spalart-Allmaras. The rotor effect is represented with an actuator disk model. The experiments have measured global rotor loads, the pressure distribution on the lower wind tunnel deflector and a portion of the velocity field downstream of the rotor itself, using a two-component PIV system.

Both experimental data and numerical solutions were obtained for several values of the rotor thrust and tunnel free stream velocity. The analysis of the numerical visualizations of the flow field and the pressure distributions on the tunnel lower deflector were used to detect the onset of flow breakdown. This has allowed to investigate the flow quality in the open section of the considered wind tunnel and also provided some hints about

the experimental indicators that may be utilized to recognize critical conditions during model rotor tests.

The structure of this paper is as follows. Section 2 describes the experimental set up and the employed measurement techniques. Section 3

summarizes the main characteristic of the CFD solver and reports the main parameters of the simulations, while the achieved experimental and numerical results are compared and discussed in section 4. Some conclusions are drawn in the last section.

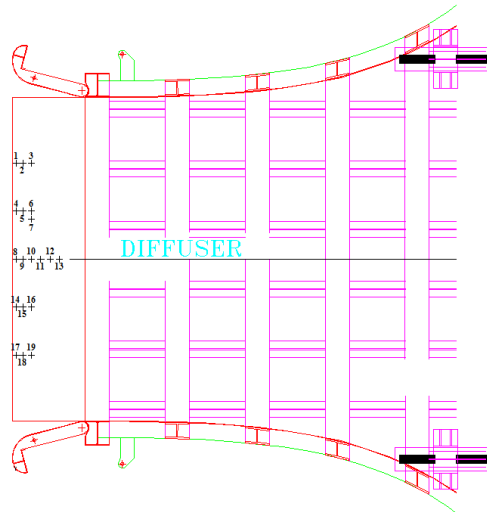


Figure 1: Pressure tap locations on the lower deflector (top view).

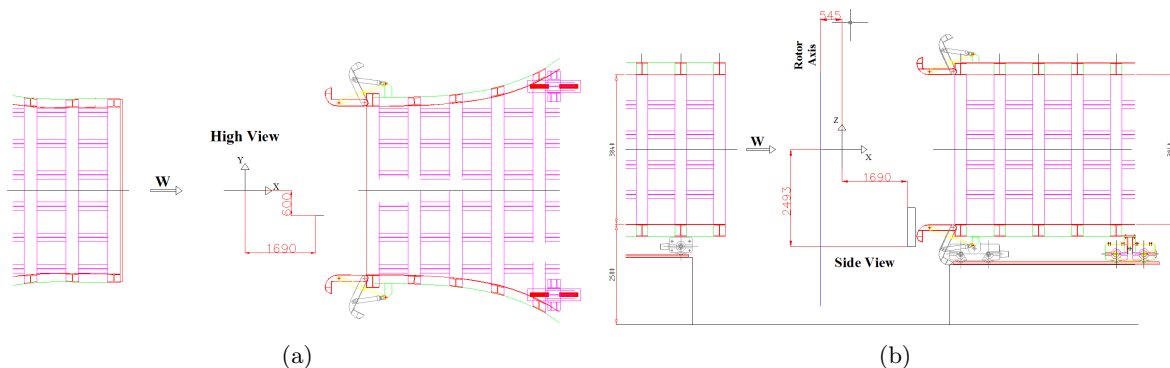


Figure 2: Location of the PIV window in the wind tunnel: (a) top view; (b) side view.

2 The experimental set up

In order to investigate the behavior of the rotor wake and its interference with the divergent portion of the wind tunnel, a limited sampling of the velocity field downstream of the rotor and the pressure distribution on the lower wind tunnel deflector were measured, together with the global rotor loads. The latter are acquired with a six-component balance mounted in the rotor hub.

The PIV system makes use of a Dantec Dynamics Nd:Yag double pulsed laser with 200 mJ output energy and a wavelength of 532 nm equipped with a 9080×0731 optical module for laser sheet and a 9080×0711 light sheet thickness adjuster; such optics combination allows to focalize the light sheet at a distance ranging between 2000 mm to 4000 mm, therefore the laser has been installed in a fixed position, by a dedicated aluminium profiles structure, on the floor

of the wind tunnel plenum, pointing to the top of the test chamber. A PCO Pixelfly double shutter CCD camera, with a 12 bit 1280×1024 pixel array, was used to acquire the image pairs. The camera is moved by a single-axis traversing system in the vertical direction in order to cover the whole measurement window, which is composed of four 200×250 mm sub-windows piled vertically. The synchronization of the emission of the two laser pulses with the exposure of the image pairs by the camera is controlled with a 6 channel Quantum Composer QC9618 pulse generator.

The PIV system is completed by two PIV-part30 particles generators by PIVTEC that feature Laskin atomizer nozzles that produce seeding consisting in small liquid droplets with diameter in the range of 1-2 μm . The particles generators have been placed in the wind tunnel diffuser and the seeding jet has been spread, by some pipes, in a narrow area with the purpose to obtain a higher density of seeding particles in the measurement plane, reducing consequently the flow seeding time and the seeding material (DEHS) consumption. The software used for images evaluation is PIVview 2C/3C developed by PIVTEC in close cooperation with the PIV-Group of the German Aerospace Center (DLR) in Gottingen and Cologne.

The PIV window is located in the downstream portion of the test section, in front of the lower deflector. It spans a rectangle of 200×1000 mm in a vertical plane parallel to the tunnel symmetry plane and located 600 mm off the symmetry axis (fig. 2). The spatial resolution of the measurements is 3.35 mm. Forty image acquisitions have been carried out for each of the four sub-windows at 1 Hz acquisition frequency.

The pressure measurements were carried out using a 32 port PSI's ESP-DTC32HD miniature pressure scanner and the pressure signals were acquired by a Pressure Systems' DTC Initium system. The pressure taps locations on the lower deflectors are reported in fig. 1. For each operating condition, four set of 100 pressure acquisitions were recorded, during the PIV sub-windows mea-

surements. All four sets were then used to compute the average and standard deviation values.

The model rotor is set at zero shaft angle, trimmed to zero flap angle and located at mid-point of the open test section, i.e. slightly upstream of the origin of the coordinate axis utilized in fig. 2.

3 The flow solver and the simulation parameters

3.1 The flow solver *ROSITA*

The *ROSITA* flow solver [4],[5] numerically integrates the RANS equations, coupled with the one-equation turbulence model of Spalart–Allmaras [6], in systems of moving, overset, multi-block grids. The equations are discretized in space by means of a cell-centred finite-volume implementation of the Roe's scheme [7]. Second order accuracy is obtained through the use of MUSCL extrapolation supplemented with a modified version of the Van Albada limiter introduced by Venkatakrisnan [8]. The viscous terms are computed by the application of the Gauss theorem and using a cell-centred discretization scheme. Time advancement is carried out with a dual-time formulation [9], employing a 2nd order backward differentiation formula to approximate the time derivative and a fully unfactored implicit scheme in pseudo-time. The generalized conjugate gradient (GCG), in conjunction with a block incomplete lower-upper preconditioner, is used to solve the resulting linear system.

To compute the low speed, steady flows considered in the present work, Turkel's [10] low Mach pre-conditioner has been employed.

The connectivity between the (possibly moving) component grids is computed by means of the Chimera technique. The approach adopted in *ROSITA* is derived from that originally proposed by Chesshire and Henshaw [11], with modifications to further improve robustness and performance.

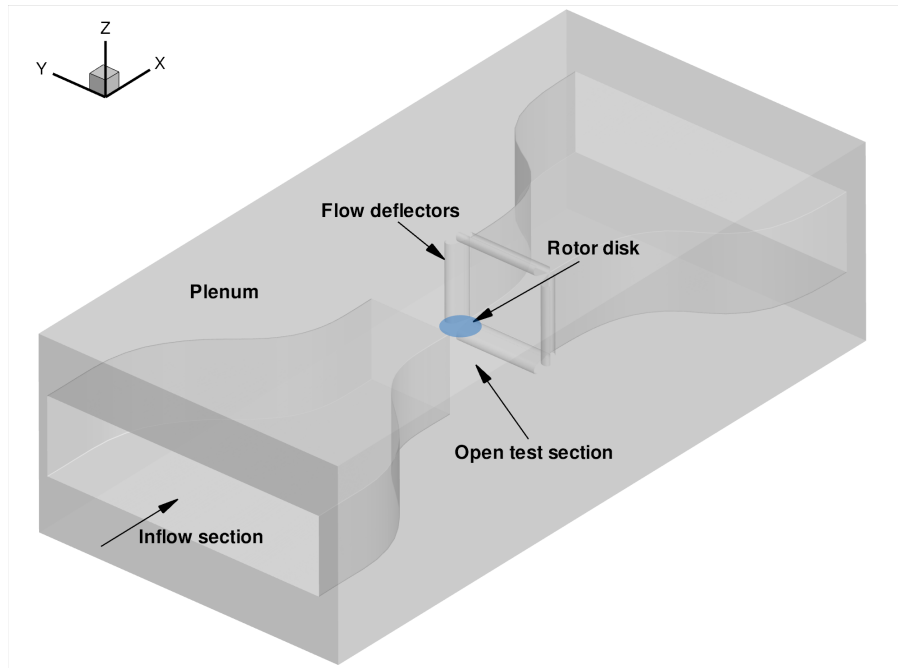


Figure 3: Numerical domain for the open test section simulations.

The domain boundaries with solid wall conditions are firstly identified and all points in overlapping grids that fall close to these boundaries are marked as holes (seed points). Then, an iterative algorithm identifies the donor and fringe points and lets the hole points grow from the seeds until they fill entirely the regions outside the computational domain. For integration of the aerodynamic forces on overlapping surface grids, a special treatment proposed by Chan and Buning [12] is used.

The *ROSITA* solver is fully capable of running in parallel on computing clusters. The parallel algorithm is based on the message passing programming paradigm and the parallelization strategy consists in distributing the grid blocks among the available processors. Each grid block can be automatically subdivided into smaller blocks by the CFD solver to attain an optimal load balancing.

3.2 The grids and the simulation parameters

Figure 3 shows the numerical domain used for the simulations of the open test section of the PoliMi large wind tunnel. The Chimera grid system consists of the following components.

- A background mesh which represents the cham-

ber containing part of the wind tunnel circuit and the open test section. The shape of the wind tunnel and the dimensions of the surrounding chamber were directly taken from a 3D CAD of the wind tunnel.

- Four grids representing the flow deflectors placed at the beginning of the wind tunnel return circuit.
- A cylindrical mesh for the actuator disk.

The figure 4 reports a slice of the computational mesh in the symmetry plane of the wind tunnel, where the different component grids can be clearly identified. In total the mesh counts about 13 million cells. The applied boundary conditions are:

- viscous wall boundary conditions on the wind tunnel walls;
- inviscid wall boundary conditions on the chamber walls;
- velocity inlet boundary conditions at the inflow section;
- pressure outlet boundary conditions at the outflow section.

The actuator disk is seen as a distribution of linear momentum sources over a disk-shaped grid plane of the cylindrical grid. The actuator disk has been positioned parallel to the wind tunnel floor since the pressure distributions on the disk where ex-

tracted from full 3D simulations of the rotor with the mast angle equal to zero and trimmed to zero flapping angle, a usual practice in the wind tunnel rotor tests.

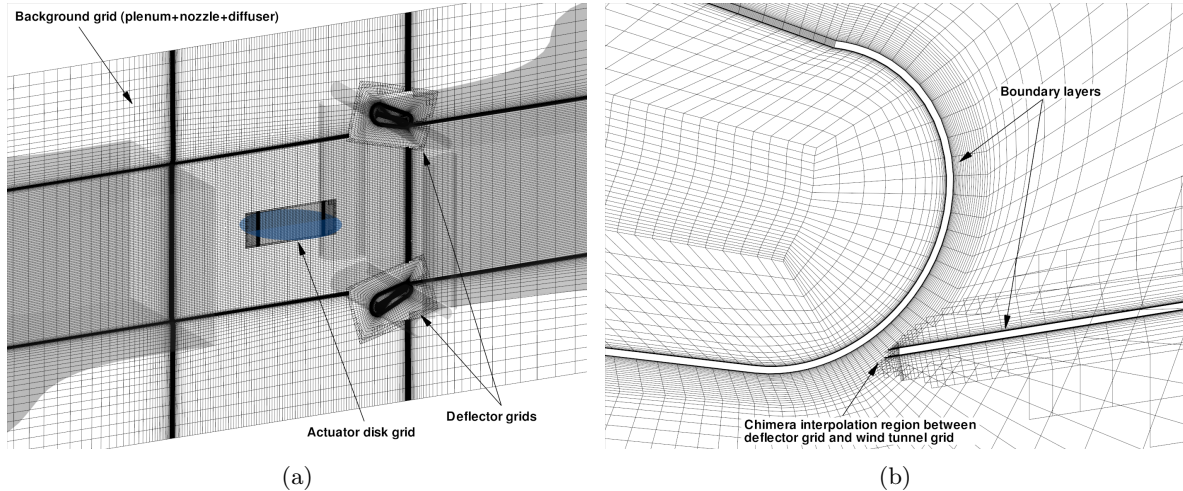


Figure 4: A slice of the computational grid in the symmetry plane of the wind tunnel (a) and a zoomed view of the slice close to the upper deflector (b).

The considered combinations of wind tunnel flow speed and rotor thrust coefficient cover the range $10 < V_\infty < 35\text{m/s}$, $0.08 < C_T/\sigma < 0.12$. The steady simulations have been performed with the RANS solver using the Spalart-Allmaras turbulence model. The solver was run in parallel on 64 processors so that 26 hours were needed to complete the 5000 iterations at $CFL = 2.5$ scheduled for each test case.

4 Analysis of results

All the selected test conditions were simulated with the assumption of a steady flow, despite the fact that unsteady phenomena are intuitively to be expected for the flow under investigation. Nevertheless, the steady solutions are retained here as a good reference to understand the overall qualitative pattern of the flow (note that an unsteady simulation of the flow would cost roughly ten times more in terms of computational time). This assumption is reasonable since we are mainly interested in the average flow in the rotor wake before

the latter possibly impinges on the tunnel walls. Unsteady flow regions are surely present after the wake impact on the tunnel walls or on the chamber floor and within the low-speed recirculation zones in the plenum, but these last mentioned regions are of less interest to us.

The above considerations become more clear if we look at figure 5, where the streamtraces of the velocity field are plotted in the region surrounding the open test section of the wind tunnel for two opposite operating conditions. At low wind tunnel speed and high disk loading the rotor wake goes downward, it partly interacts with the lower flow deflector and then it is convected in the chamber right below the return circuit of the wind tunnel, promoting the onset of regions of unsteady, low speed, recirculating flow. At high speed and low disk loading the wake is instead completely ingested in the return circuit.

In the following, some experimental data will be utilized to validate the numerical model. Then additional computations will be used to obtain an overall picture of the flow field quality within the tunnel at different operating conditions.

test	V_∞ (m/s)	C_T/σ
1	20	0.10
2	15	0.10
3	10	0.08
4	10	0.12

Table 1: Experimental operating conditions used in the comparison

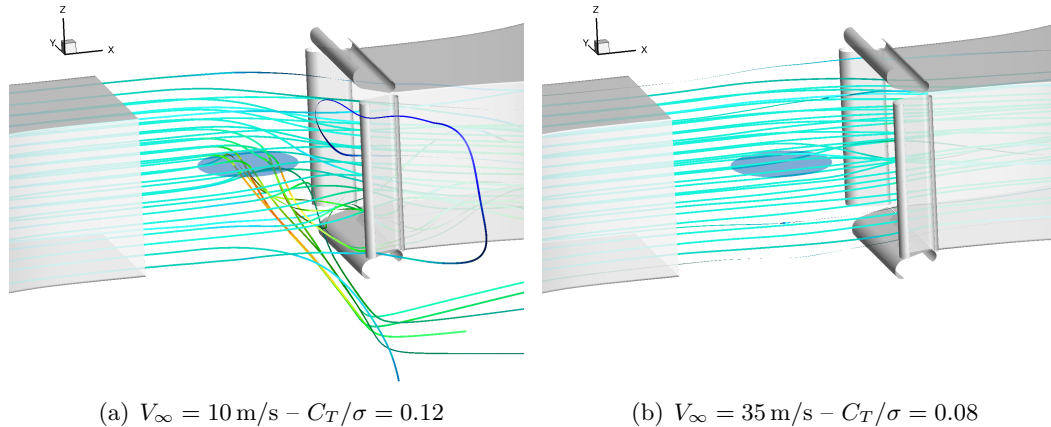


Figure 5: Streamtraces of the velocity field.

4.1 Comparison with experiments

Experimental data are available for comparison at selected values of the tunnel velocity and rotor thrust coefficient, as specified in table 1.

At the higher considered tunnel velocity, $V_\infty = 20$ m/s ($C_T/\sigma = 0.10$), the wake is entirely laying in the tunnel duct, as visualized by the computed two-component velocity magnitude plotted in the PIV window plane in fig. 6(a). The open jet is bent downwards by the presence of the rotor and impinges on the low deflector. The velocity magnitude within the PIV window is enlarged in figures 6(b) (numerical) and 6(c) (experimental). In the same plots pseudo-streamtraces are shown. Both experimental and numerical velocity fields are influenced by the upstream effect of the lower deflector. Although the overall velocity values and in-plane velocity direction in the window are similar, in the experimental data the local effect of the deflector is felt at a larger distance from the chamber ground.

When decreasing the tunnel velocity at the same thrust (fig. 6(d)), the wake inclination increases so as, in the experimental case, to enter the PIV window, as shown in fig. 6(f). This is how-

ever not the case for the numerical results, which predict a wake average location still above the window itself, with corresponding streamtraces which are less bent downwards.

At $V_\infty = 10$ m/s, $C_T/\sigma = 0.08$ (fig. 7(a)) the computed wake is observable within the PIV window. The experimental data show again a higher wake inclination, with somewhat unexpected high velocity values.

Finally, at $V_\infty = 10$ m/s, $C_T/\sigma = 0.12$ (fig. 7(d)), the rotor wake largely escape from the tunnel. In the computation, the PIV window lies in the inner part of the wake, featuring lower velocity values. The experimental data suggest that the wake is flowing fully outside of the tunnel.

Additional information can be gathered from the comparison of the pressure distributions on the lower deflector, shown in fig. 8. The continuous contours represent the numerical results, while the dots represent the experimental data. Note that the pressure scales are different for the different operating conditions, for clarity reasons.

At $V_\infty = 20$ m/s the calculations predict a symmetrical pressure distribution, which is almost the case also in the experimental data. The stan-

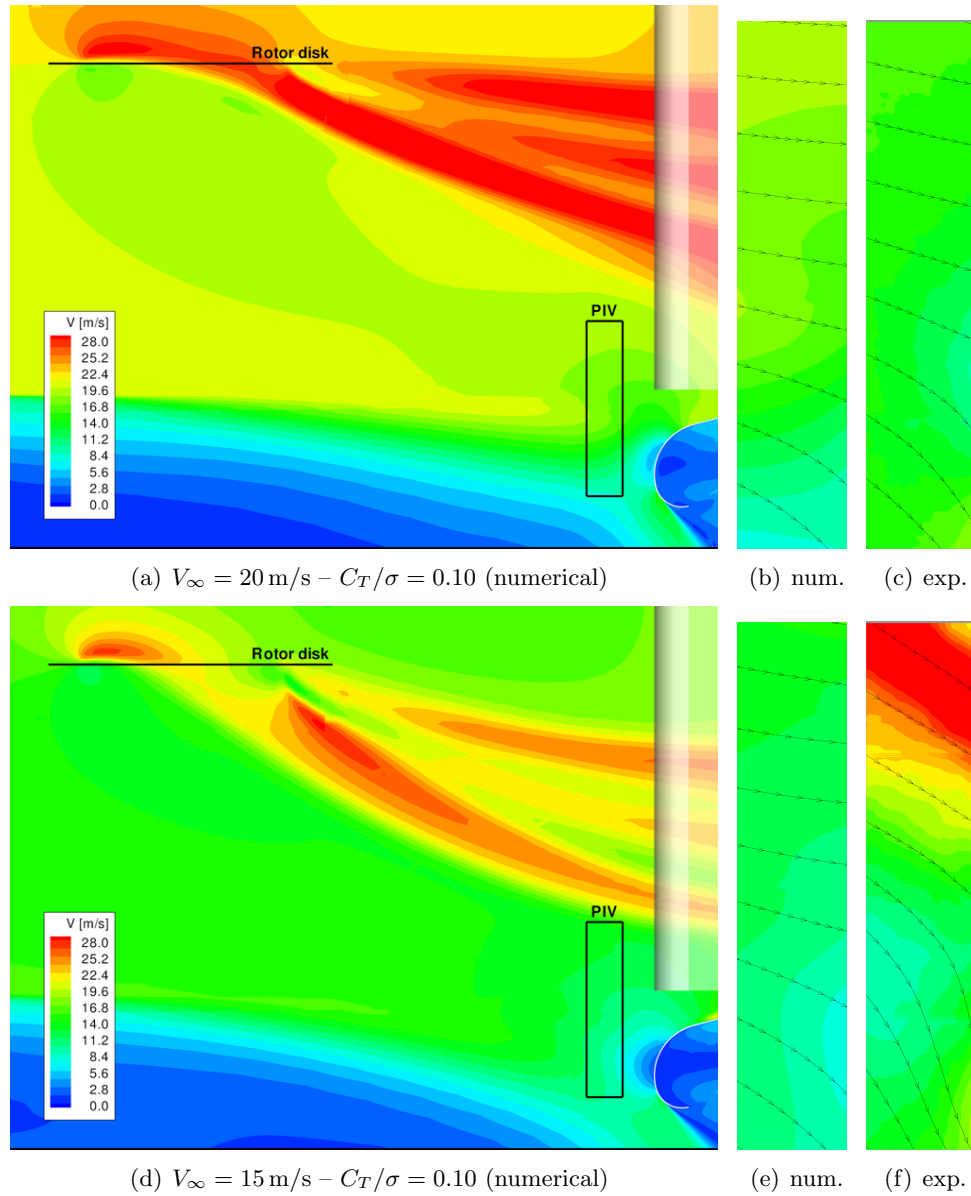


Figure 6: Two-component velocity field in the measuring vertical off-axis plane: the right part of the figure reproduce the PIV window. a),b),c) $V_\infty = 20 \text{ m/s} - C_T/\sigma = 0.10$; d),e),f) $V_\infty = 15 \text{ m/s} - C_T/\sigma = 0.10$

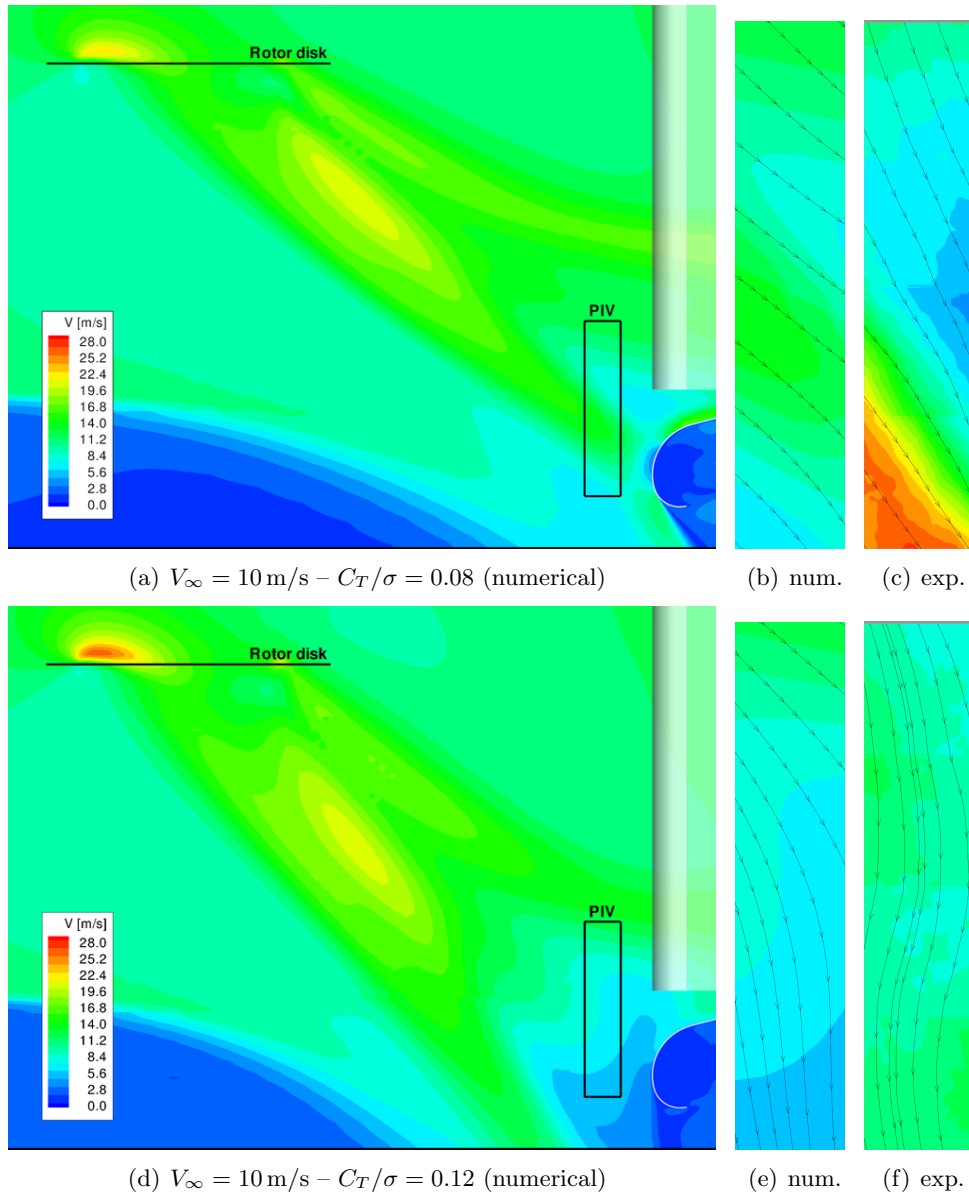


Figure 7: Two-component velocity field in the measuring vertical off-axis plane: the right part of the figure reproduce the PIV window. a),b),c) $V_\infty = 10 \text{ m/s} - C_T/\sigma = 0.08$; d),e),f) $V_\infty = 10 \text{ m/s} - C_T/\sigma = 0.12$

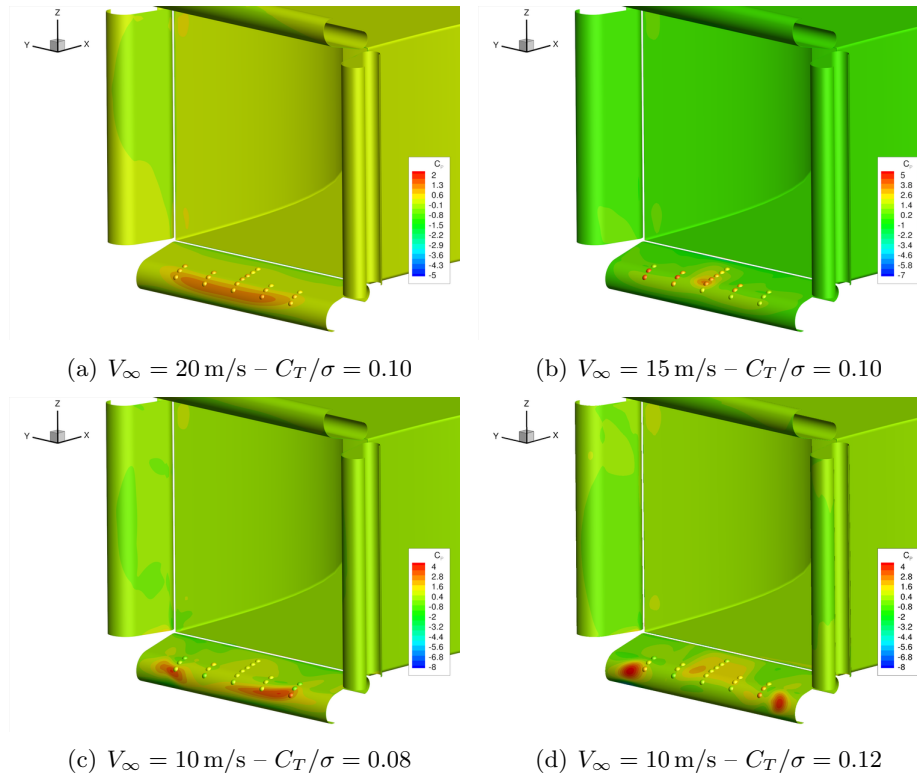


Figure 8: Pressure coefficient distribution on the lower deflector

standard deviation of the pressure measurements in this operating conditions is less than 8 %, indicating a smooth flow on the lower deflector.

At $V_\infty = 15 \text{ m/s}$ we can observe a quite good matching of the pressure in the tunnel centerline, but the calculations fail in predicting the asymmetrical experimental distribution. This may be caused by the lack of swirl in the AD computed wake. The standard deviation of the measurements increase to 21 %, indicating an increased unsteadiness of the flow on the lower deflector.

At the lower tunnel velocity, $V_\infty = 10 \text{ m/s}$, the computed pressure distribution indicates the impingement of the main wake vortices on the deflector at both thrust values considered (figures 8(c) and 8(d)), by the presence of high pressure spots on the side portions of the deflector itself. This is partially confirmed by the experimental measurements, especially at $C_T/\sigma = 0.12$, which also feature at the side rows pressure sensors a value of the standard deviation larger than 100 %.

4.2 Flow breakdown analysis

In this section a purely numerical investigation is carried out to span a larger range of tunnel operating conditions, with the aim of analyzing the possible occurrence of flow breakdown in the tunnel open test section. The flow field is visualized utilizing the Mach number distributions in the tunnel symmetry plane.

The trajectory of the wake for four operating conditions is visualized in fig. 9. The same figure allows to appreciate the effect of the rotor on the wind tunnel nozzle jet. At low wind tunnel speeds the jet is significantly bent downward and, consequently, part of the jet flows outside the wind tunnel circuit and, at the same time, there is a suction of low speed fluid in the upper part of the divergent section. It is important to note, however, that the low speed fluid does not interact with the rotor disk, at least in the considered range of wind tunnel speeds. In fact, by the analysis of the presented numerical solutions it seems that, for all the considered speeds and rotor thrusts, the flow in the neighborhood of the rotor disk is qualitatively similar to that of the free-flight flow.

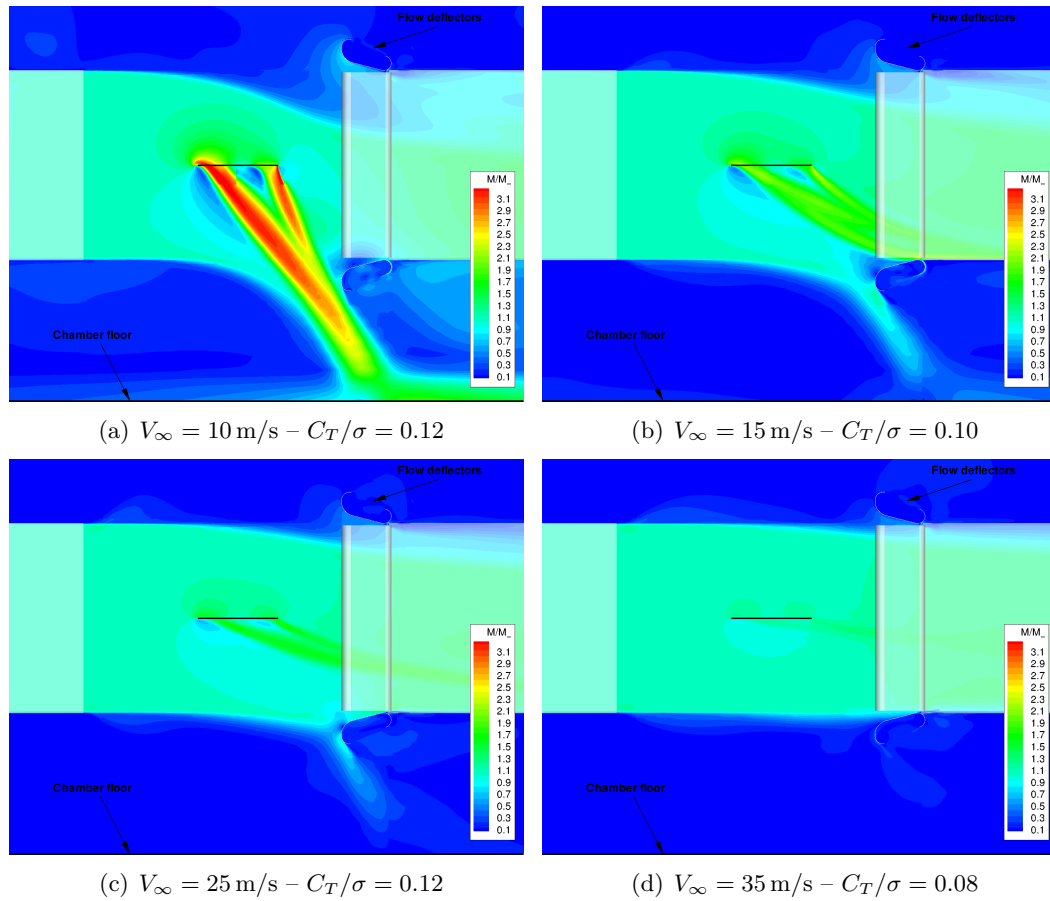


Figure 9: Mach number distribution in the vertical symmetry plane of the open test section (normalized with respect to the Mach number at the exit of the wind tunnel nozzle).

Indeed, there is no evident interaction of the rotor with its own wake or with the shear layer of the nozzle jet, even for the lowest velocities and the highest disk loading. The only noticeable effect, observed for an intermediate range of velocities and thrust coefficients, is the impact of the wake on the lower deflector, which may cause an unsteady ground effect. The presented numerical results suggest that this unsteady phenomenon could appear for $V_\infty \leq 25$ m/s.

In order to detect the proximity of such conditions during wind tunnel operation, it is desirable to devise a (simple) means to detect the position of the rotor wake. As suggested also by the experiments, pressure measurements may be among the simplest means to estimate the trajectory of the rotor wake. In figure 10 the pressure coefficient distribution on the wind tunnel walls is plotted beside the distribution of the Mach number in the test section vertical symmetry plane for $V_\infty = 10$ m/s and for various rotor thrusts.

The analysis of the figure reveals that when the wake is impacting on the lower deflector one or more pressure peaks can be observed on the deflector surface. Considering the rotor operating condition range, the distribution of the pressure in terms of the location where the wake impact on the deflector can be summarized as follows:

- For $V_\infty = 10$ m/s and $C_T/\sigma = 0.12$ the wake escapes almost completely the wind tunnel inlet but there is no reingestion of the wake by the rotor (see figure 10(c)). The effect of the wake impingement on the lower deflector are two pressure peaks on the side portion of the leading edge of the deflector, reasonably due to the two main vortices generated by the roll-up of the wake. For lower velocities and higher thrusts it is expected that the wake does not interact any more with the deflector and it is entirely pushed down into the space between the wind tunnel lower wall and the chamber floor.
- For the operating conditions between ($V_\infty = 10$ m/s, $C_T/\sigma = 0.10$) and ($V_\infty = 15$ m/s, $C_T/\sigma = 0.08$), the two pressure peaks coalesce into a single peak located roughly in the middle (in the y direction) of the deflector surface. The peak moves from the leading edge to the trailing edge as the velocity is increased or as the thrust is decreased. In these operating conditions a ground effect due to the interaction between the wake and the deflector could arise.
- For $V_\infty > 20$ m/s the wake enters completely the return circuit of the tunnel, and only a slight pressure raise distributed over the leading edge of the lower deflector may be noticed.

From the above description stems that it is possible to monitor the rotor wake position by measuring the pressure at some selected locations on the lower deflector.

5 Conclusions

An extensive qualitative numerical analysis of the flow inside the open test section of the Politecnico di Milano large wind tunnel in the presence of rotor effects has been carried out, supplemented by a selected amount of experimental measurements. The flow has been simulated with the flow solver *ROSITA*, adopting an actuator disk model of the AW139 rotor to account for the rotor effects in the numerical solution. The measurements have included global rotor loads, pressures on the lower tunnel deflector and PIV data in a 200×1000 mm window.

Direct comparison of velocity fields in the PIV window and pressure distributions on the lower deflector indicates the limitations of the present numerical model based on the AD representation of the model rotor. The computations underestimate the wake inclination with respect to the experimental indications at a given tunnel velocity and thrust level. A better agreement is found for the pressure distributions.

Nonetheless, the numerical simulations have allowed to analyze a large range of tunnel operating conditions. The computed flow fields in the open test section appeared to be similar to the flow field of the rotor in free-flight conditions for all the operating conditions of interest.

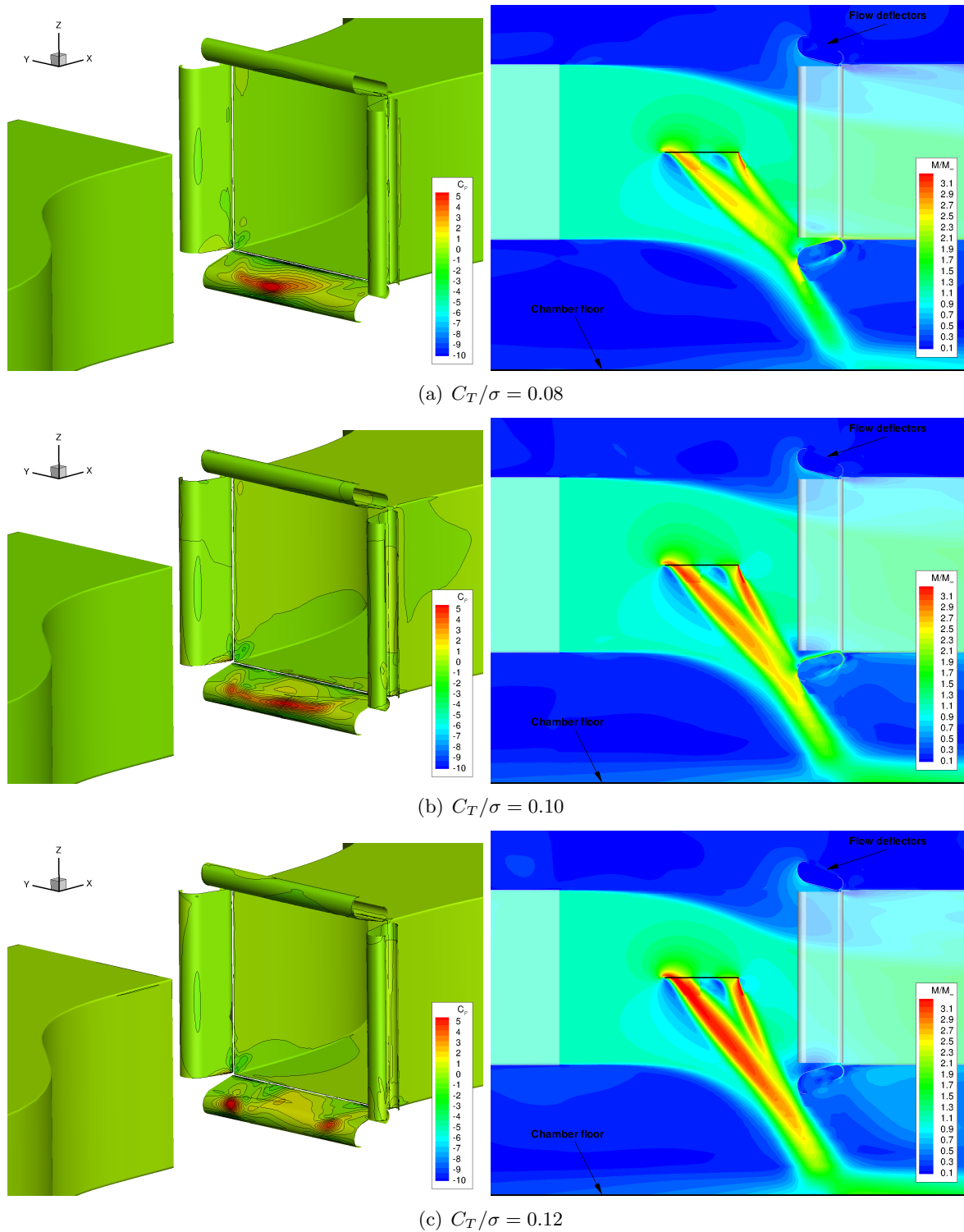


Figure 10: Pressure coefficient distribution on the tunnel walls (left) and Mach number distribution in the vertical symmetry plane of the test section (right) for $V_\infty = 10$ m/s.

Quantitative effects on the measured performance are however to be expected, due to the unsteady interaction of the rotor wake with the wind tunnel walls, and the operating parameters range where the phenomenon could occur have been identified. A practical means to detect these critical conditions during the actual wind tunnel operations has been given, based on pressure measurement at some selected locations of the lower deflector.

Acknowledgements: this work has been carried out in the framework of Project WITCH (Wind Tunnel Correction methodology for model rotor tests), funded by AWPARC.

References

- [1] J.-J. Philippe. Consideration on wind-tunnel testing techniques for rotorcrafts. In *AGARD Special Course on Aerodynamics of Rotorcraft*, 1990.
- [2] P. M. Shinoda. Wall interaction effects for a full-scale helicopter rotor in the NASA Ames 80- by 120-foot wind tunnel. In *AGARD Meeting on "Wall Intereference, Support Intereference and Flow Field Measurements"*, 1993.
- [3] H.J. Langer, R.L. Peterson, and T.H. Maier. An Experimental Evaluation of Wind Tunnel Wall Correction Methods for Helicopter Performance. In *American Helicopter Society 52nd Annual Forum Proceedings*, 1996. Washington, DC.
- [4] M. Biava. *RANS computations of rotor/fuselage unsteady interactional aerodynamics*. PhD thesis, Dipartimento di Ingegneria Aerospaziale, Politecnico di Milano, 2007.
- [5] M. Biava, W. Khier, and L. Vigevano. CFD prediction of air flow past a full helicopter configuration. *Aero. Sci. Tech.*, 19:3–18, 2012.
- [6] P.R. Spalart and S.R. Allmaras. One equation model for aerodynamic flows. In *30th AIAA Aerospace Science Meeting & Exhibit, Reno, NV. AIAA 92-0439*, 1992.
- [7] P.L. Roe. Approximate Riemann Solvers, Parameter Vectors and Difference Schemes. *J. Comp. Phys.*, 43:357–372, 1981.
- [8] V. Venkatakrishnan. On the accuracy of limiters and convergence to steady state solutions. In *31st AIAA Aerospace Sciences Meeting and Exhibit, Reno, NV. AIAA 93-0880*, 1993.
- [9] A. Jameson. Time dependent calculations using multigrid with applications to unsteady flows past airfoils and wings. In *10th AIAA Computational Fluid Dynamics Conference, Honolulu, HI. AIAA 91-1596*, 1991.
- [10] E. Turkel, R. Radespiel, and N. Kroll. Assessment of preconditioning methods for multidimensional aerodynamics. *Computers & Fluids*, 6:613–634, 1997.
- [11] G. Chesshire and W. D. Henshaw. Composite overlapping meshes for the solution of partial differential equations. *J. Comp. Phys.*, 90:1–64, 1990.
- [12] W. M. Chan and P. G. Buning. Zipper grids for force and moment computation on overset grids. *AIAA Paper*, (95-1681-CP), 1995.